

IRS 9: The Case for a Dynamically-Ejected Star from the Galactic Center

MATTHEW W. HOSEK JR.,^{1,*} TUAN DO,¹ SMADAR NAOZ,^{1,2} SANAEA C. ROSE,³ GREGORY D. MARTINEZ,¹ ANDREA M. GHEZ,¹ REBECCA LEWIS-MERRILL,¹ JESSICA R. LU,⁴ SHOKO SAKAI,¹ AND JAY ANDERSON⁵

¹ *UCLA Department of Physics and Astronomy, Los Angeles, CA 90095*

² *Mani L. Bhaumik Institute for Theoretical Physics, Department of Physics and Astronomy, UCLA, Los Angeles, CA 90095, USA*

³ *Center for Interdisciplinary Exploration and Research in Astrophysics (CIERA), Northwestern University, 1800 Sherman Ave, Evanston, IL 60201*

⁴ *Department of Astronomy, 501 Campbell Hall, University of California, Berkeley, CA, 94720*

⁵ *Space Telescope Science Institute, 3700 San Martin Drive, Baltimore, MD 21218, USA*

ABSTRACT

Measuring stellar motions at the Milky Way’s Galactic center (GC) provides unique insight into the dynamical processes within galactic nuclei. We present proper motion measurements for 23 SiO-maser emitting stars within 45" of SgrA*, including four previously reported to have velocities exceeding their local escape velocities (i.e., they are “locally unbound” from the GC). Derived from 14 epochs of HST WFC3-IR observations (2010 – 2023), our measurements have a median precision of 0.038 mas yr⁻¹ – up to \sim 100x more precise than previous constraints for some sources. By combining these proper motions with published radial velocities, we derive updated 3D velocities for the masers and find that only one is locally unbound (IRS 9; $v_{3d} = 370 \pm 1.2$ km s⁻¹). Orbit integrations place the first constraints on the orbit of IRS 9, which is bound to the GC at larger radii with $r_{peri} \geq 0.100 \pm 0.005$ pc and $r_{apo} \geq 5.25 \pm 0.18$ pc. IRS 9’s high velocity relative to stars at similar radii in the Nuclear Star Cluster makes it a candidate to have experienced a strong dynamical interaction in order to place it on its orbit. We explore the Hills mechanism as a possible origin, but binary evaporation and ejection velocity limits indicate that IRS 9 is unlikely to have experienced such an event in the past 0.4 Myr (the timescale constrained by the orbit integrations). Alternative mechanisms that could produce IRS 9 include binary supernova disruption, two-body interactions, and stellar collisions. Identifying additional stars like IRS 9 will be essential for understanding these various dynamical processes.

Keywords: Galactic Center, Astrometry

1. INTRODUCTION

Due to its proximity, the Milky Way’s Galactic center (GC) is the only galactic nucleus for which it is possible to study the kinematics of individual sources in great detail. As such, the GC provides a window into the stellar populations within a galactic nucleus and the dynamical processes that act upon them. Measurements of stellar orbits at the GC have proven the existence of a central supermassive black hole (SMBH) with a mass of \sim 4 x10⁶ M_⊙ associated with the emissive source SgrA* (e.g. Schödel et al. 2002; Ghez et al. 2003, 2008; Gillessen et al. 2009; Do et al. 2019; GRAVITY Collab-

oration et al. 2022). Surrounding SgrA* is the Nuclear Star Cluster (NSC), the densest and most massive star cluster in the Galaxy, which is composed of primarily old stars (\gtrsim 5 Gyr) with a total mass of \sim 10⁷ M_⊙ within R \lesssim 5 pc (e.g. Schödel et al. 2014; Chatzopoulos et al. 2015; Schödel et al. 2020; Gallego-Cano et al. 2020; Chen et al. 2023). Similar components have been found in the nuclei of many galaxies beyond the Milky Way (e.g. Kormendy & Ho 2013; Neumayer et al. 2020; Fahrion et al. 2024), and so the GC offers a template for understanding these complex systems.

SiO masers provide useful probes of stellar kinematics of this region. A component of the NSC population, stars with SiO maser emission are evolved red giant or supergiant stars with extended circumstellar envelopes that produce emission lines at radio wavelengths associated with SiO molecules (e.g. Reid 2002; Kemball 2007).

Corresponding author: Matthew W. Hosek Jr.
mwwhosek@astro.ucla.edu

* Brinson Prize Fellow

Because of their value in defining an astrometric reference frame for studies of stellar orbits at the GC (e.g. Menten et al. 1997; Ghez et al. 2008; Plewa et al. 2015; Sakai et al. 2019), these sources have been the target of long-running radio campaigns to measure their proper motions and radial velocities to high precision (Reid et al. 2003, 2007; Li et al. 2010; Paine & Darling 2022; Darling et al. 2023; Tsuboi et al. 2025).

Interestingly, four of the 25 known stellar masers near SgrA* ($r_{2d} \leq 45''$, where r_{2d} is the projected radius on the sky) have been reported to be “locally unbound”, i.e., they exhibit velocities that exceed the escape velocities at their projected radii from SgrA* according to GC mass models. The star IRS 9 was the first maser source identified to be locally unbound on the basis of its large radial velocity (Reid et al. 2007). Three additional masers were identified as being locally unbound by Paine & Darling (2022, hereafter P22) on the basis of their large proper motions (SiO-16, SiO-21, and SiO-25). The presence of so many high-velocity sources within this limited sample raises the question of what dynamical mechanism(s) might be responsible for producing them.

In this paper, we report proper motion measurements for 23 of the stellar SiO masers near SgrA*, including the four proposed high-velocity sources, derived using multi-epoch Hubble Space Telescope (HST) observations of the GC (14 epochs between 2010 – 2023). These proper motions are combined with radial velocities in the literature to calculate updated 3D velocities for the masers (§2), which are then compared to the GC escape velocity curve to identify sources that are locally unbound (§3.1). We then use orbit integrations to place the first constraints on the orbit of IRS 9, which is found to be bound to the GC at larger radii (§3.2). The velocity and orbital eccentricity of IRS 9 is compared to the expected distributions for stars in the NSC (§4.1), and dynamical mechanisms that might have accelerated IRS 9 on its current orbit are explored (§4.2). Finally, we summarize our findings in §5.

2. OBSERVATIONS AND MEASUREMENTS

2.1. HST Astrometry and Proper Motions

The HST observations and procedure for extracting astrometric measurements used in this work are described in (Hosek et al. 2025, hereafter H25)¹. Briefly, 14 epochs of WFC3-IR observations of a 2' x 2' field centered on SgrA* ($\alpha(\text{J2000}) = 17^h 45^m 40.04^s$, $\delta(\text{J2000}$

$= -29^\circ 00' 28''.10$) were obtained using the F153M bandpass filter between 2010.6261 – 2023.6178 (see Table 1 from H25). Stellar photometry and astrometry is extracted in a two-step process. First, the FORTRAN routine `img2xym_wfc3ir` (a precursor to the package `hst1pass` described in Anderson 2022) is used for an initial round of star detection in each image using a library of spatially-variable point-spread functions (PSFs) for the WFC3-IR F153M filter. For each image, a perturbation is applied to the PSFs to minimize the PSF residuals and a first-order polynomial transformation is used to align the image into a common reference frame defined for the epoch. Second, the FORTRAN routine `KS2` (Anderson et al. 2008; Bellini et al. 2017, 2018) is used to combine the individual images into a combined image for the epoch, run source detection on that combined image, and then extract measurements for the detected sources back in the individual images. This allows for significantly deeper source detection than is possible in the first step alone.

This process produces a starlist with the astrometric and photometric measurements for each epoch. The astrometric uncertainty of a given star is calculated as the error-on-the-mean of its measured positions across the individual images within the epoch ($\sigma_{HST} = \sigma_{img} / \sqrt{N_{img}}$, where σ_{HST} is the astrometric error and σ_{img} is the standard deviation of the positions across N_{img}). The photometric uncertainty is calculated as the standard deviation of the instrumental magnitudes measured across the images within the epoch (see Hosek et al. 2015). Instrumental magnitudes are transformed into Vega magnitudes using the `KS2` zeropoints from Hosek et al. (2018). A typical starlist in the dataset contains $\sim 50,000$ stars and extends to a depth of F153M ~ 22.5 mag (the 95th percentile of the extracted magnitudes).

Proper motions are derived as described in H25. First, the HST astrometry for each epoch is transformed into the Gaia-CRF3 reference frame (Gaia Collaboration et al. 2022), which is tied to the International Celestial Reference System (ICRS; Arias et al. 1995). Stars are then cross-matched between epochs and proper motions are calculated using a method that uses Gaussian Processes to simultaneously model systematic correlations in the astrometry (see section 3.2 of H25). Finally, the proper motions are transformed into a SgrA*-at-Rest frame (a reference frame where SgrA* is at the position origin and is at rest) using the ICRS position and proper motion of SgrA* from Xu et al. (2022). Overall, the astrometric transformations between these reference frames incur a systematic error of (0.025, 0.019) mas yr^{-1} in the ($\mu_{\alpha*}$ and μ_{δ}) proper motions and (0.213,

¹ All the HST data used in this paper can be found in MAST: doi:10.17909/vre6-c497

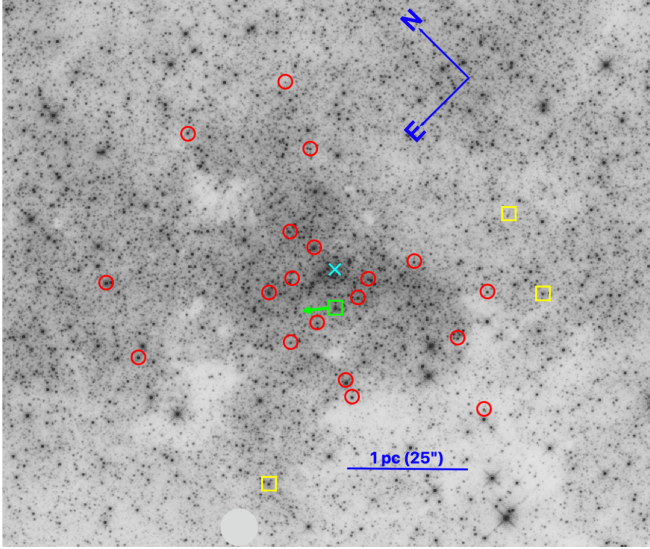


Figure 1. The 23 SiO masers examined in this study, overlaid on an HST F153M image. The green square represents IRS 9, which is found to exhibit a velocity larger than the maximum escape velocity at its radius (i.e., it is locally unbound from the GC). The green arrow shows the direction of its HST proper motion (not to scale). The yellow squares correspond to three masers proposed to be locally unbound (SiO-16, SiO-21, and SiO-25), but the new HST proper motions indicate that they do not exceed their maximum escape velocities. The red circles show the positions of the other masers in the sample. All sources have projected distances of $R \leq 45''$ (~ 1.8 pc) from SgrA* (cyan x).

0.471) mas in the (α^*, δ) positions². These systematic errors are added in quadrature with the measurement errors to get the final proper motion errors. The best-measured stars in the dataset achieve proper motion errors of ~ 0.03 mas yr^{-1} (H25).

2.2. Identifying Masers and Calculating Their 3D Velocities

We identify HST counterparts to a sample of 25 SiO masers within $r_{2d} \leq 45''$ ($r_{2d} \lesssim 1.8$ pc) of SgrA* that have radio-based proper motion measurements (P22, see also Darling et al. 2023, hereafter D23). The radio proper motions are used to calculate the expected positions of the masers at a time of 2015.5, and the HST proper motion are used to do the same for the HST sources. An HST source is matched with a maser if its position is consistent with the radio position to within a matching radius of $0.15''$ and if the reduced chi-squared

statistic of the HST kinematic motion model fit (χ^2_{red}) is less than 5 (a conservative quality cut to eliminate poorly fit HST sources, see H25). This results in successful matches for 23 of the 25 masers, including all 4 proposed locally unbound sources (Figure 1). The two unmatched sources are SiO-12, for which no HST source was found within the matching radius, and SiO-17, which did have an HST source within the matching radius but with a poor HST kinematic motion model fit ($\chi^2_{red} > 5$), likely due to the influence of a nearby bright star biasing the astrometry.

The 3D velocities of the masers (v_{3d}) are calculated by combining their HST proper motions with the radial velocities from P22³. These radial velocities are reported in the local standard of rest (LSR), which we assume to be equivalent to their radial velocity relative to SgrA* (i.e., SgrA* has no significant line-of-sight motion with respect to the LSR and is at rest relative to the dynamical center of the Milky Way; Reid & Brunthaler 2004, 2020). To convert the proper motions from angular to physical units, we assume a distance to SgrA* of 8.1 kpc (the average of recent distance estimates; Do et al. 2019; GRAVITY Collaboration et al. 2022).

A catalog of the masers with HST proper motions and updated 3D velocities is provided in Appendix A. The masers vary in brightness between $10.95 \text{ mag} \leq \text{F153M} \leq 17.73 \text{ mag}$ and their proper motion measurements have a median uncertainty of $0.038 \text{ mas yr}^{-1}$. For the masers closest to SgrA* ($r_{2d} \leq 20''$, or $r_{2d} \lesssim 0.8$ pc), the HST measurements achieve similar uncertainties as previous radio-based studies, as these sources have been extensively monitored via radio observations (Reid et al. 2003, 2007; Li et al. 2010; Paine & Darling 2022; Darling et al. 2023). For sources at larger radii ($r_{2d} \geq 20''$, or $r_{2d} \gtrsim 0.8$ pc), the HST measurements improve the uncertainties by as much as ~ 100 x relative to radio-based measurements. This is because there is often significantly more HST astrometry available for the sources at large radii compared to radio studies (e.g. Paine & Darling 2022). A detailed comparison between the HST and radio proper motion measurements for the masers is provided Appendix B.

3. RESULTS

3.1. Are the Masers Locally Unbound From the GC?

We compare the 3D velocities of the masers to the escape velocities at their projected radii (r_{2d}) to determine

² Note that α^* is used to designate the RA coordinate projected on a tangent plane on the sky, i.e. $\text{RA} \cos(\text{DEC})$, while δ is used to designate the DEC coordinate.

³ We use the radial velocities from P22 because they report uncertainties on the radial velocities while D23 do not. Regardless, the P22 and D23 radial velocities are consistent within 0.4 km/s, which is well within the uncertainties of the 3D velocities.

if they are locally unbound from the GC. Since the line-of-sight distances of the masers are not well constrained, r_{2d} represents the minimum possible physical radius of a given source from SgrA*. Thus, the escape velocity at r_{2d} is the maximum possible escape velocity for that source ($v_{esc,max}$). A maser is locally unbound if it fulfills the condition:

$$v_{3d} \geq v_{esc,max} \quad (1)$$

$$v_{esc,max} = \sqrt{2GM_{enc}/r_{2d}},$$

where v_{3d} is the 3D velocity of the maser, M_{enc} is the enclosed mass within r_{2d} , and G is the gravitational constant (e.g. Reid et al. 2003).

To calculate M_{enc} , we adopt a mass model for the GC with two components: the supermassive black hole (SMBH), which dominates the gravitational potential for $r \lesssim 1$ pc, and the Nuclear Star Cluster (NSC), which dominates between 1 pc $\lesssim r \lesssim 30$ pc (e.g. Launhardt et al. 2002; Sormani et al. 2020). We adopt a SMBH mass of $(4.14 \pm 0.16) \times 10^6 M_{\odot}$, which represents the average and standard deviation of the masses reported by Do et al. (2019) and GRAVITY Collaboration et al. (2022). For the NSC, we adopt the mass density distribution from the best-fit axisymmetric model from Chatzopoulos et al. (2015, see their Equations 17 and 19):

$$\rho(R, z) = \frac{3 - \gamma}{4\pi q} \frac{a_{NSC} M_{NSC}}{m^{\gamma} (m + a_{NSC})^{4-\gamma}}, \quad (2)$$

where

$$m^2 = R^2 + \frac{z^2}{q^2}, \quad (3)$$

and $R = \sqrt{x^2 + y^2}$, $q = 0.73 \pm 0.04$, $\gamma = 0.71 \pm 0.12$, $a_{NSC} = 5.9 \pm 1.07$ pc, and $M_{NSC} = (6.1 \pm 0.3) \times 10^7 M_{\odot}$.

At a given r_{2d} , the uncertainty in $v_{esc,max}$ is calculated via a Monte-Carlo simulation. We draw 100 samples of the SMBH mass and NSC model parameters, each perturbed by a random amount drawn from a Gaussian distribution with a width equal to its uncertainty, and then calculate $v_{esc,max}$ for each sample. The uncertainty in $v_{esc,max}$ is calculated as the standard deviation of the values across the samples.

We find that only IRS 9 has a 3D velocity that is significantly above $v_{esc,max}$ at its projected radius (Figure 2). At $r_{2d} = 0.33$ pc, IRS 9 exhibits $v_{3d} = 370.4 \pm 1.2$ km s $^{-1}$ compared to $v_{esc,max} = 331.1 \pm 6.5$ km s $^{-1}$. This corresponds to a difference at the 5.9σ significance level (where σ is the combined uncertainty in v_{3d} and $v_{esc,max}$), indicating that IRS 9 is locally unbound.

However, the remaining masers in the HST sample have 3D velocities below their $v_{esc,max}$ limits, including the proposed high-velocity sources SiO-16, SiO-21, and

SiO-25 (Figure 2). The updated v_{3d} values for these masers are over ~ 1000 km s $^{-1}$ lower than those reported in P22, representing the largest discrepancies between the HST and radio measurements by far (Appendix B). P22 note that the radio-based proper motions for these sources are derived from very limited radio astrometry (only 2 epochs over a ~ 2 year time baseline), and so the HST proper motion measurements are likely to be more reliable.

For later discussion of possible dynamical mechanisms for IRS 9 (§4.2), it is useful to convert the star's observed velocity into the velocity at infinity relative to the SMBH ($v_{\infty,smbh}$; the velocity at infinity if only the SMBH is considered for the gravitational potential). Assuming the minimum possible physical radius of IRS 9 (i.e., its physical radius is equal to its projected radius $r_{2d} = 0.33$ pc), then the observed velocity corresponds to $v_{\infty,smbh} = 134 \pm 18$ km s $^{-1}$. This represents a lower limit for $v_{\infty,smbh}$, because if the true physical radius of IRS 9 is larger, then the corresponding $v_{\infty,smbh}$ would also be larger (Appendix C).

It should be noted that the 3D velocity of IRS 9 is dominated by its large radial velocity of -341 ± 1.2 km s $^{-1}$ (P22). There is no evidence of significant radial velocity variations for IRS 9 across many epochs of radio observations (Reid et al. 2007, P22), and independent near-infrared spectroscopy of the star yields similar radial velocity values (Zhu et al. 2008). This suggests that the radial velocity we adopt for IRS 9 is reasonable.

3.2. Constraints on the Orbit of IRS 9

While IRS 9 is locally unbound, it is not necessarily destined to escape the GC. This is because of the extended mass distribution in the region; as the radius of IRS 9 increases, then the amount of enclosed mass also increases. Thus, it is possible for IRS 9 to become bound at a larger radius and follow an orbit rather than a hyperbolic trajectory.

We use `galpy` (Bovy 2015) to integrate the orbit of IRS 9 in the GC gravitational potential in order to place the first constraints on its periapse, apoapse, and orbital eccentricity. The gravitational potential is taken to be a multi-component model containing the SMBH, NSC, and Nuclear Stellar Disk (which dominates for $r \gtrsim 30$ pc) derived via axisymmetric Jeans modeling of the region (Model 2 from Sormani et al. 2020). For IRS 9, 5 out of 6 phase space parameters are known, with measurements of its 3D velocity and the 2D projected position on the sky. However, the star's distance along the line-of-sight not well constrained (d_{los} , which we define as distance along the line-of-sight relative to SgrA*). For these calculations we will assume that $d_{los} = 0$ pc (i.e.,

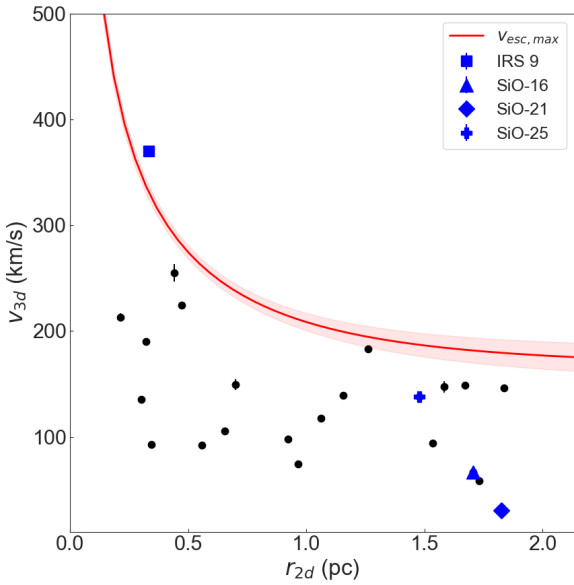


Figure 2. Maser v_{3d} as a function of r_{2d} . A model for $v_{esc,max}$ and the corresponding 1σ uncertainty in that model is shown by the red line and shaded region. Previously reported masers with $v_{3d} > v_{esc,max}$ are highlighted by blue markers: IRS 9 (blue square), SiO-16 (blue triangle), SiO-21 (blue diamond), and SiO-25 (blue plus sign). When the HST proper motions are used, only IRS 9 has $v_{3d} > v_{esc,max}$.

the projected radius is equal to the physical radius), which produces the “tightest” possible orbit that IRS 9 can have. In other words, constraints on the periape and apoapse of the $d_{los} = 0$ pc orbit represent lower limits of their true values (see Appendix C).

To quantify the impact of measurement uncertainties on the orbit constraints, we resample the projected position and 3D velocity of IRS 9 for 500 iterations, each time using new values drawn from Gaussian distributions with means and standard deviations equal to the different measurements and their corresponding uncertainties. An orbit is calculated for each iteration that extends 0.4 Myr into the past, at which point the orbit constraints become weak due to the growing impact of the measurement uncertainties over time (Figure 3). This timescale captures the three previous orbits of IRS 9, which has an average orbital period (i.e., the time between successive periape or apoapse passages) of 0.11 ± 0.005 Myr across the iterations.

The resulting orbits reveal that IRS 9 must be on a highly eccentric orbit if $d_{los} = 0$. For the three most recent orbits captured in this analysis, the periape distances (r_{peri}) are 0.100 ± 0.005 pc, 0.25 ± 0.02 pc, and 0.14 ± 0.02 pc, in order of most recent to fur-

thest back in time. The corresponding apoapse distances (r_{apo}) are 5.25 ± 0.18 pc, 5.42 ± 0.16 pc, and 5.24 ± 0.20 pc. So, the eccentricities of the orbits ($e = (r_{apo} - r_{peri})/(r_{apo} + r_{peri})$) are 0.96 ± 0.001 , 0.91 ± 0.006 , and 0.95 ± 0.008 .

We reiterate that these values for r_{peri} and r_{apo} are lower limits as they increase if $|d_{los}|$ increases (Appendix C). Thus, for purposes of exploring possible dynamical mechanisms for IRS 9 (§4.2), we conclude that IRS 9 could not have come closer than 0.100 ± 0.005 pc to SgrA* in the past 0.4 Myr.

4. DISCUSSION

4.1. Are the Kinematics of IRS 9 Unusual for a Star in the NSC?

To explore the dynamical origin of IRS 9, we first evaluate if its kinematics are unusual for a star in the NSC. We define the probability of observing a star with a velocity greater than or equal to a given v_{3d} as:

$$P_{NSC} = \int_{v_{3d,i}}^{\infty} D(v_{3d}, r) dv_{3d}, \quad (4)$$

where $D(v_{3d}, r)$ is the probability distribution of v_{3d} at the radius r of the star within the NSC. $D(v_{3d}, r)$ is assumed to follow a Maxwellian distribution with a scale parameter equal to $\sigma_{1d}(r)$ (the 1D velocity dispersion at r), as is the case for a stellar isothermal sphere (e.g. Binney & Tremaine 2008).

To calculate P_{NSC} for IRS 9, we assume that $\sigma_{1d} = 113$ km s $^{-1}$ at its radius based on the best-fit dynamical models of the NSC from Chatzopoulos et al. (2015). The corresponding Maxwellian distribution provides a reasonable match for the observed v_{3d} distribution for a sample of 32 stars with radii within $\pm 1''$ of IRS 9’s projected radius ($7.5'' \leq r_{2d} \leq 9.5''$, corresponding to 0.29 pc $\lesssim r_{2d} \lesssim 0.37$ pc), excluding IRS 9 itself (Figure 4). Stellar proper motions and radial velocities are obtained from the catalogs of H25 and Feldmeier-Krause et al. (2017), respectively. These stars exhibit stellar colors consistent with stars found near the GC (F127M - F153M > 2.6 mag, e.g. H25).

Under these assumptions, we calculate that $P_{NSC} \sim 1\%$ to observe a star with v_{3d} equal to that of IRS 9 at its projected radius. While this does not conclusively identify IRS 9 as a velocity outlier within the NSC, it shows that it is a candidate to have experienced a significant dynamical interaction (or several such interactions) in order to eject it from the GC and place it on its current orbit. Based on an analysis of stellar velocities for stars within $r_{2d} \lesssim 20''$, Tripe et al. (2008) argue that IRS 9 does not exhibit an excessively high velocity as several stars in their sample exhibit $v_{3d} > 358$ km

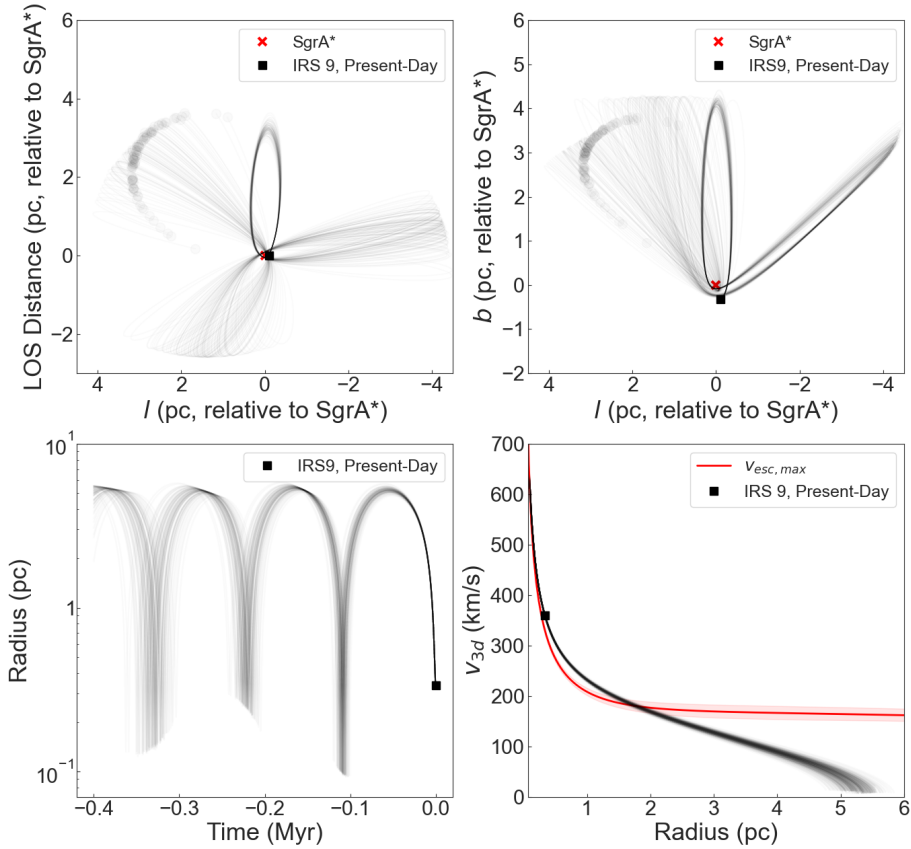


Figure 3. The orbit of IRS 9, integrated for the past 0.4 Myr and assuming $d_{los} = 0$ pc. In each panel, the black lines represent orbits drawn from an MC simulation over the measured properties of IRS 9, and so the spread of lines reveals the uncertainty in the orbit. Top left: A “top-down” view of the orbit from the North Galactic Pole (with Earth at negative LOS distance). The solid black square represents the current position of IRS 9 while the faded black circles represent the end point of each orbit (i.e., 0.4 Myr in the past). SgrA* is represented by the red “x”. Top right: An “edge-on” view of the orbit from the Galactic Plane, constructed in the same manner as the top-left panel. Bottom left: The distance of IRS 9 from SgrA* as a function of time. Bottom right: The v_{3d} of IRS 9 as a function of radius, compared to $v_{esc,max}$ (red line with uncertainty shown as shaded region). IRS 9 is locally unbound when $v_{3d} > v_{esc,max}$, as is the case at the present-day (at $r_{2d} = 0.33$ pc). However, the star is bound to the GC at larger radii as v_{3d} drops below $v_{esc,max}$.

s^{-1} . However, their sample spans a range of radii, and since the velocity dispersion of the NSC increases with decreasing radius (e.g. Trippe et al. 2008; Chatzopoulos et al. 2015), then stars with smaller radii than IRS 9 can be expected to exhibit higher velocities. Among the sample of stars examined here with similar radii to IRS 9, the highest velocity is $339.6 \pm 2.0 \text{ km s}^{-1}$, which is $\sim 30 \text{ km s}^{-1}$ slower than the observed velocity of IRS 9 (Figure 4).

Whether IRS 9 is a true velocity outlier relative to the NSC is sensitive to the assumptions made regarding $D(v_{3d}, r)$, especially at the high-end tail of the distribution. A detailed dynamical analysis of the NSC is re-

quired to rigorously model $D(v_{3d}, r)$ but is beyond the scope of this paper.

4.2. Possible Dynamical Mechanisms

Given the high density of stars in the GC as well as the presence of an SMBH, there are several dynamical mechanisms that may have acted upon IRS 9 to place it on its current orbit. Based on the observed velocity of IRS 9 and the constraints on its orbit, we explore whether IRS 9 could have been produced by the Hills Mechanism (§4.2.1), binary disruption via supernova (§4.2.2), or a close two-body interaction/stellar collision (§4.2.3).

4.2.1. The Hills Mechanism

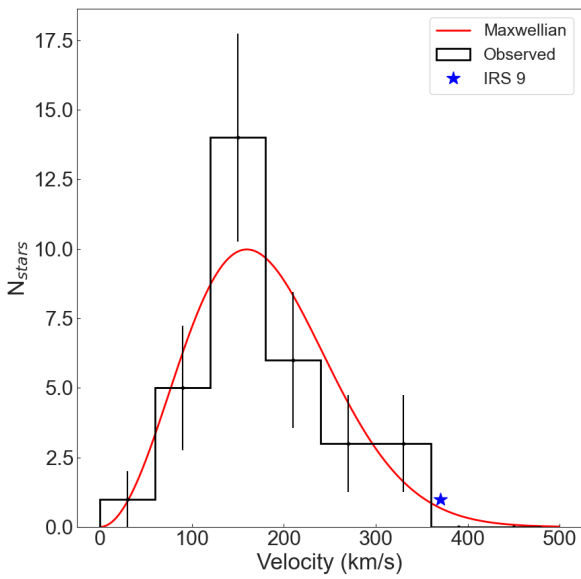


Figure 4. The observed $v3d$ distribution of 32 stars with projected radii within $\pm 1''$ of IRS 9 (black histogram), compared to the $v3d$ of IRS 9 itself (blue star). The expected $v3d$ distribution of the NSC is taken to be a Maxwellian distribution with a scale parameter equal to the velocity dispersion at this radius derived from a dynamical model of the NSC (Chatzopoulos et al. 2015, red line). From this distribution, we calculate that the probability of observing a star with a $v3d$ greater or equal to IRS 9 is $\sim 1\%$.

The Hills mechanism, which describes the disruption of a binary when it passes close enough to an SMBH that the gravitational tidal force on the binary exceeds its binding energy, has been long identified as a mechanism to eject stars from galactic nuclei (Hills 1988, see also review by Brown (2015)). This process has been invoked to explain the existence of hypervelocity stars, which exhibit velocities large enough to escape the Galaxy (e.g. Koposov et al. 2020). However, it is expected to produce stars at a wide range of velocities depending on the properties of the initial binary star system (e.g. Kenyon et al. 2008; Rossi et al. 2014; Generozov & Madigan 2020; Verberne et al. 2025). If IRS 9 was ejected by the Hills Mechanism within the past 0.4 Myr (the timescale where the orbit is constrained by the analysis in §3.2), then the breakup of its initial binary is likely to have occurred at the periape of the orbit at $r \sim 0.1$ pc. To determine if this is a viable scenario, we explore the possible configurations of this initial binary and evaluate (1) its lifespan in the dense GC environment, and (2)

the ejection velocity that would be achieved by a Hills disruption.

We begin by estimating the age and mass of IRS 9 and its hypothetical binary companion. As a SiO maser source, IRS 9 is likely an thermally-pulsating Asymptotic Giant Branch star (TPAGB) with a dynamic circumstellar atmosphere (e.g. Habing 1996; Kemball 2007). The evolved nature of IRS 9 indicates that it is part of the old stellar population of the NSC. While the star formation history and metallicity distribution of the NSC is debated, recent studies suggest that the cluster is dominated by metal-rich stars ($[Z] \sim 0.5$) with ages between $\sim 5 - 10$ Gyr, with smaller sub-populations of metal-poor stars ($[Z] \sim -1.0$) at similar ages and/or an intermediate-aged population at ~ 3 Gyr (e.g. Schödel et al. 2020; Chen et al. 2023). Thus, we assume that the initial binary system containing IRS 9 formed at least $\gtrsim 3$ Gyr ago.

Stellar evolution models predict that TPAGB stars in stellar populations spanning the age and metallicity range found in the NSC would have masses between $1 M_\odot - 2 M_\odot$ (Choi et al. 2016). We adopt this as the likely mass range for IRS 9. For the binary companion, we explore two limiting cases: one case where $M_{irs9} / M_{comp} = 1$, in which IRS 9 and the companion star are the same mass, and another where $M_{irs9} / M_{comp} = 0.1$, in which IRS 9 is the secondary to a massive $10 M_\odot - 20 M_\odot$ primary star. This spans the range of mass ratios typically observed for binary star systems ($0.1 \leq q \leq 1$; Sana et al. 2012; Moe & Di Stefano 2017).

In order to undergo a Hills mechanism disruption at a given radius from SgrA* ($r_{disrupt}$), the semi-major axis (a_{bin}) of the binary system would be:

$$a_{bin} \sim r_{disrupt} \left(\frac{m_b}{3M_{bh}} \right)^{1/3}, \quad (5)$$

where m_b is the total mass of the binary, and M_{bh} is the mass of SgrA* (e.g. Brown 2015). As before, M_{bh} is assumed to be $4.14 \times 10^6 M_\odot$. Assuming $r_{disrupt} = 0.1$ pc, this calculation yields $162 \text{ AU} \lesssim a_{bin} \lesssim 204 \text{ AU}$ for the $M_{irs9} / M_{comp} = 1$ system and $286 \text{ AU} \lesssim a_{bin} \lesssim 360 \text{ AU}$ for the $M_{irs9} / M_{comp} = 0.1$ system.

There are two challenges to this scenario. First, the large separations mean that the binary lifetime, due to interactions with neighboring stars, is very short. Second, the resultant velocity of an ejected star due to the Hills mechanism of such a binary is too slow to produce a star with the velocity observed for IRS 9. We discuss these two issues below.

1. Binary Evaporation Timescale — Due to the high stellar density and velocity dispersion at the GC, binaries are prone to evaporation, a process by which they

are gravitationally disrupted by repeated encounters by passing stars (e.g. Alexander & Pfahl 2014). Following Rose et al. (2020), we calculate the orbit-averaged binary evaporation timescale (t_{ev}) for possible IRS 9 binaries (see their Equation 16). For this calculation, we assume that the original binary system was on the same highly-eccentric orbit as IRS 9 today (§3.2). This provides an upper limit on t_{ev} , since the initial binary system was presumably on a lower eccentricity orbit than what IRS 9 (as the ejected component) exhibits today, and t_{ev} generally increases with increasing eccentricity as more time is spent at larger radii from SgrA*. Under this formulation, we find that the evaporation timescale of the $M_{irs9} / M_{comp} = 1$ binary system with $r_{disrupt} = 0.1$ pc would be $\lesssim 20$ Myr. This is at least 150x smaller than the current age of IRS 9, and so such a system could not have survived long enough to experience a Hills mechanism disruption in the past 0.4 Myr (Figure 5).

For a $M_{irs9} / M_{comp} = 0.1$ binary system, the binary disruption timescale is not set by evaporation but by the stellar evolution of the primary star. The MIST stellar evolution models predict that a $10 M_{\odot}$ star at $[Z] = 0.5$ (e.g., the massive companion to IRS 9) will evolve to a supernova in ~ 30 Myr (Choi et al. 2016). This becomes the upper limit on the disruption timescale of such systems, independent of the radius of the binary relative to SgrA*. Therefore, this type of system also could not have survived long enough to disrupt in the past 0.4 Myr (Figure 5).

2. *Ejection Velocity* — The velocity of a star ejected via the Hills mechanism (at infinity, relative to the SMBH) is:

$$v_{\infty,smbh} = \alpha \sqrt{\frac{2Gm_c}{a_{bin}}} \left(\frac{M_{bh}}{m_b} \right)^{1/6}, \quad (6)$$

where m_c is the mass of the captured star and α is a constant that three-body scattering experiments indicate is on the order of unity (e.g. Sari et al. 2010; Rossi et al. 2014; Verberne et al. 2025). The $v_{\infty,smbh}$ of IRS 9 increases as the mass of its hypothetical companion (which would be captured by SgrA* in the Hills scenario) increases. However, even for a $M_{irs9} / M_{comp} = 0.1$ system, $v_{\infty,smbh} \sim 75 \text{ km s}^{-1}$ at $r_{disrupt} = 0.1$ pc, which is significantly lower than the observed value of $v_{\infty,smbh} \geq 134 \pm 18 \text{ km s}^{-1}$ (Figure 5).

To summarize, it is highly unlikely that the Hills mechanism could have produced IRS 9 within the past 0.4 Myr (the timescale covered by the orbit calculations)

due to timescale and ejection velocity arguments.⁴ To invoke the Hills mechanism, the initial binary containing IRS 9 would need to have been disrupted within ~ 30 Myr of its formation and at $r_{disrupt} < 0.1$ pc. Investigating whether such an event could produce a star with a present-day orbit that is consistent with IRS 9 is beyond the scope of this paper.

4.2.2. *Binary Disruption via Supernova*

Another dynamical mechanism that could accelerate stars to high velocities is the disruption of stellar binary systems due to supernova (SNe). In this case, a companion to a massive star can become unbound due to the sudden mass loss as well as a natal kick from the SNe itself (e.g. Blaauw 1961; Hansen & Phinney 1997; Hobbs et al. 2005). This mechanism is expected to be active at the GC, where it is estimated that only $\lesssim 10\%$ of massive binary systems will evaporate before the first SNe occurs (Lu & Naoz 2019; Jurado et al. 2024). Simulations predict that between 0.5% (Hoang et al. 2022) and 10% (Bortolas et al. 2017) of such systems within $r \lesssim 0.1$ pc from SgrA* will result in the secondary companion becoming unbound from the SMBH, with that percentage rising to as high as $\sim 20\%$ when binaries at larger radii are considered (with most ejections occurring between $0.1 \leq r \leq 0.5$ pc; Zubovas et al. 2013). The ejection velocities of these stars can be quite high (up to $\sim 2000 \text{ km s}^{-1}$ for closely bound systems at $r = 0.1$ pc; Hoang et al. 2022), and so the observed velocity of IRS 9 ($v_{\infty,smbh} \gtrsim 134 \pm 18 \text{ km s}^{-1}$) can certainly be achieved.

Similar to the Hills mechanism, the SNe disruption scenario would need to occur soon after the formation of the initial binary, as the SNe of the massive companion would be expected to occur within $\lesssim 30$ Myr. Whether IRS 9 could have been ejected early on via this mechanism and then evolve to its present-day orbit requires additional analysis that is beyond the scope of this paper.

4.2.3. *Close Two-Body Interactions/Stellar Collisions*

Close two-body interactions and stellar collisions are active dynamical mechanisms near the GC due to the high stellar densities in the region. It is predicted that close two-body encounters could eject stars at velocities similar to what is found for IRS 9 ($v_{\infty,smbh} \gtrsim 130 \text{ km s}^{-1}$) at a rate between $\sim 10^{-4} \text{ yr}^{-1}$ and $\sim 10^{-5} \text{ yr}^{-1}$ from

⁴ We note that this conclusion also holds in the extreme case of a $M_{irs9} / M_{comp} = 10$ binary system, where IRS 9 has a $0.1 M_{\odot} - 0.2 M_{\odot}$ companion. For such a system, the binary evaporation time is even faster ($\lesssim 15$ Myr) and the $v_{\infty,smbh}$ from Hills is even lower ($\sim 16 \text{ km s}^{-1}$) at $r_{disrupt} = 0.1 \text{ pc}$.

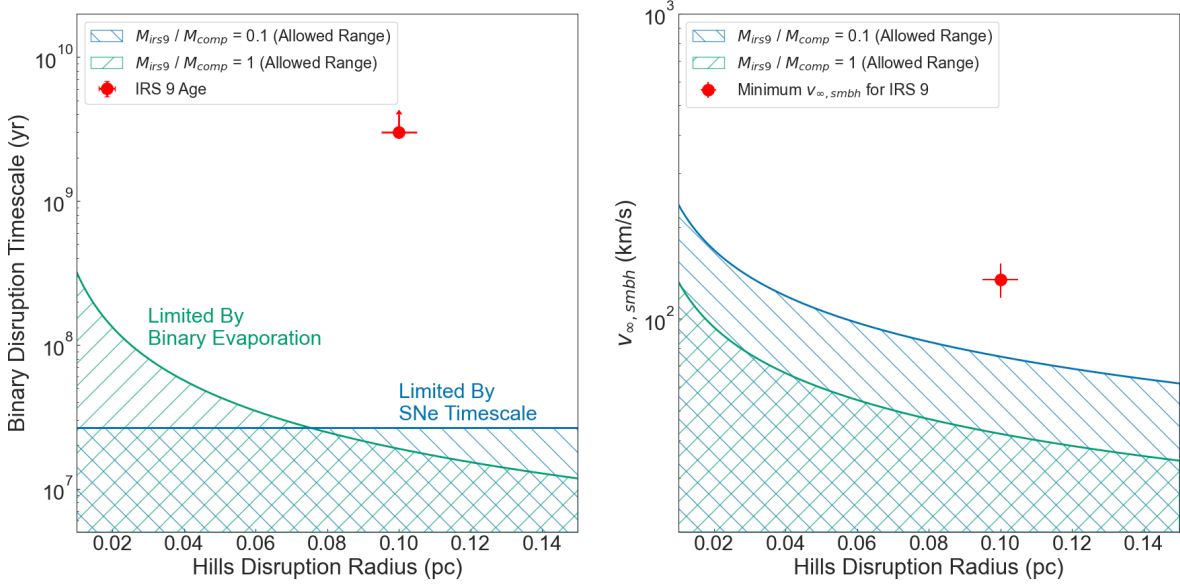


Figure 5. Binary disruption timescale (left) and $v_{\infty, \text{smbh}}$ (right) as a function of Hills disruption radius for hypothetical binary systems containing IRS 9. The allowed ranges for a $M_{\text{irs9}} / M_{\text{comp}} = 1$ system (green hashed region) and a $M_{\text{irs9}} / M_{\text{comp}} = 0.1$ system (blue hashed region) are shown, as well as the current values for IRS 9 (red points). Assuming that the Hills disruption occurred at the minimum periape of IRS 9’s current orbit ($r_{\text{peri}} = 0.1$ pc), the disruption timescales of the binary systems are $\lesssim 30$ Myr. Given IRS 9’s current age of $\gtrsim 3$ Gyr, the binary systems could not survive long enough to disrupt within the past 0.4 Myr. Further, the binary systems cannot achieve the minimum $v_{\infty, \text{smbh}}$ of IRS 9 (134 ± 18 km s $^{-1}$, calculated assuming $|d_{\text{los}}| = 0$ pc) via the Hills mechanism at a disruption radius of 0.1 pc.

the GC (Yu & Tremaine 2003). Stellar collisions are also thought to be an important dynamical mechanism in the region, with the ability to modify the stellar population (e.g. Dale et al. 2009; Mastrobuono-Battisti et al. 2021; Balberg & Yassur 2023; Zhang et al. 2023; Rose et al. 2023; Balberg 2024) and radial density distribution (e.g. Rose & MacLeod 2024). Recent simulations indicate that such collisions can produce “unbound” stars (that is, stars unbound from the SMBH) with $v_{\infty, \text{smbh}}$ values similar to IRS 9 due to collisions that occur at $R \sim 0.1$ pc from SgrA* (Rose & Mockler 2025). The rate of such ejections could also be as high as $\gtrsim 10^{-5}$ yr $^{-1}$, depending on the assumptions made regarding energy dissipation during the collisions (e.g. Rose et al. 2025). However, the rate at which these mechanisms might produce stars with velocities similar to IRS 9 is not well constrained by observations.

5. CONCLUSIONS

We present proper motion measurements for 23 SiO masers near SgrA* ($r_{2d} < 45''$, or $r_{2d} \lesssim 1.8$ pc) derived from 14 epochs of HST WFC3-IR observations of the GC obtained between 2010 – 2023. These measurements are independent of previous radio-based proper motions of these sources (P22; D23) and are often more

precise, by as much as a factor of ~ 100 for masers at larger radii ($r_{2d} > 20''$). We combine the HST proper motions with radial velocities for the sources from the literature in order to calculate their total velocities (v_{3d}) and compare them to the escape velocities at the GC at their projected radii ($v_{\text{esc}, \text{max}}$). This comparison reveals that only IRS 9 exhibits $v_{3d} > v_{\text{esc}, \text{max}}$, indicating that it must be locally unbound from the GC ($v_{3d} = 370 \pm 1.2$ km s $^{-1}$, corresponding to $v_{\infty, \text{smbh}} \gtrsim 134 \pm 18$ km s $^{-1}$). None of the other masers in the sample meet the criteria of being locally unbound, including previously proposed high-velocity candidates SiO-16, SiO-21, and SiO-25.

While IRS 9 is locally unbound, it is not necessarily destined to escape the GC as a whole. Assuming that its physical radius is equal to its projected radius of $r_{2d} = 0.33$ pc (i.e., $d_{\text{los}} = 0$ pc), we integrate the motion of IRS 9 for the past 0.4 Myr in the GC gravitational potential to place the first constraints on its orbit. We find that IRS 9 is on a bound orbit with $r_{\text{peri}} \geq 0.100 \pm 0.005$ pc and $r_{\text{apo}} \geq 5.25 \pm 0.18$ pc, with an eccentricity $e \geq 0.91 \pm 0.006$ over this time. We estimate that the probability of observing a star with a velocity greater than or equal to that of IRS 9 in the NSC at its projected radius is $\sim 1\%$, identifying it as a candidate to have

experienced a significant dynamical interaction to place it on its current orbit.

Given the observed velocity of IRS 9 and the constraints on its orbit, we explore whether the star could have been produced by the Hills Mechanism. In this scenario, IRS 9 originated in a binary system that was tidally disrupted by a dynamical interaction with SgrA*. Assuming that the disruption occurred in the past 0.4 Myr (the timescale constrained by the orbit analysis), then the binary was likely destroyed near the periape distance of 0.1 pc. For the range of probable IRS 9 binary systems in this scenario, we find binary evaporation timescale is too short for the system to survive long enough to be disrupted in the past 0.4 Myr, and further, that expected ejection velocity of IRS 9 would be too slow to explain its velocity today. Therefore, if IRS 9 were produced by the Hills mechanism then its initial binary must have been destroyed soon after its formation ($\lesssim 30$ Myr) and at a radius < 0.1 pc.

Alternative dynamical mechanisms at the GC that could produce stars with velocities similar to that observed for IRS 9 include binary disruption via SNe, two-body interactions, and stellar collisions. If IRS 9 were ejected via the SNe of a massive companion, then the event also must have occurred within ~ 30 Myr of its formation due to the stellar evolution timescale of the companion. Two-body interactions and stellar collisions have been predicted to eject stars from the GC with velocities similar to that of IRS 9, although the rate of such events is uncertain. Future studies are required to determine which (if any) of these mechanisms is most likely to have acted upon IRS 9. Moving forward, constraining the population of high-velocity/locally unbound stars near the GC will allow us to better understand these various dynamical mechanisms and the rate at which they occur.

ACKNOWLEDGMENTS

The authors thank Elena Rossi for valuable discussions regarding possible dynamical mechanisms for IRS 9, as well as the referee whose comments improved this paper. M.W.H. is supported by the Brinson Prize Fellowship. S.C.R. thanks the Lindheimer Postdoctoral Fellowship for support. S.N. acknowledges the partial support of NSF-BSF grant AST-2206428, as well as Howard and Astrid Preston for their generous support. A.M.G. acknowledges support from her Lauren B. Leichtman and Arthur E. Levine Endowed Astronomy Chair, as well as from the Gordon E. & Betty I. Moore Foundation (award #11458) and GC Star Society. This work is based on observations made with the NASA/ESA Hubble Space Telescope, obtained at the Space Telescope Science Institute, which is operated by the Association of Universities for Research in Astronomy, Inc., under NASA contract NAS 5-26555. The observations are associated with programs GO-11671, GO-12318, GO-12667, GO-13049, GO-15199, GO-15498, GO-16004, GO-15894, GO-16681, and GO-16990. This research has made extensive use of the NASA Astrophysical Data System.

Facilities: HST (WFC3-IR)

Software: AstroPy ([Astropy Collaboration et al. 2013](#)), galpy ([Bovy 2015](#)), Matplotlib ([Hunter 2007](#)), numPy ([Harris et al. 2020](#)), KS2 ([Anderson et al. 2008](#)), SciPy ([Virtanen et al. 2020](#))

REFERENCES

Alexander, T., & Pfuhl, O. 2014, *ApJ*, 780, 148

Anderson, J. 2022, One-Pass HST Photometry with *hst1pass*, Instrument Science Report WFC3 2022-5, 55 pages,

Anderson, J., Sarajedini, A., Bedin, L. R., et al. 2008, *AJ*, 135, 2055

Arias, E. F., Charlot, P., Feissel, M., & Lestrade, J. F. 1995, *A&A*, 303, 604

Astropy Collaboration, Robitaille, T. P., Tollerud, E. J., et al. 2013, *A&A*, 558, A33

Balberg, S. 2024, *ApJ*, 962, 150

Balberg, S., & Yassur, G. 2023, *ApJ*, 952, 149

Bellini, A., Anderson, J., Bedin, L. R., et al. 2017, *ApJ*, 842, 6

Bellini, A., Libralato, M., Bedin, L. R., et al. 2018, *ApJ*, 853, 86

Binney, J., & Tremaine, S. 2008, *Galactic Dynamics: Second Edition* (Princeton University Press)

Blaauw, A. 1961, *BAN*, 15, 265

Bortolas, E., Mapelli, M., & Spera, M. 2017, *MNRAS*, 469, 1510

Bovy, J. 2015, *ApJS*, 216, 29

Brown, W. R. 2015, *ARA&A*, 53, 15

Chatzopoulos, S., Fritz, T. K., Gerhard, O., et al. 2015, *MNRAS*, 447, 948

Chen, Z., Do, T., Ghez, A. M., et al. 2023, *ApJ*, 944, 79

Choi, J., Dotter, A., Conroy, C., et al. 2016, *ApJ*, 823, 102

Dale, J. E., Davies, M. B., Church, R. P., & Freitag, M. 2009, *MNRAS*, 393, 1016

Darling, J., Paine, J., Reid, M. J., et al. 2023, *ApJ*, 955, 117

Do, T., Hees, A., Ghez, A., et al. 2019, *Science*, 365, 664

Fahrion, K., Böker, T., Perna, M., et al. 2024, *arXiv e-prints*, arXiv:2404.08910

Feldmeier-Krause, A., Kerzendorf, W., Neumayer, N., et al. 2017, *MNRAS*, 464, 194

Gaia Collaboration, Klioner, S. A., Lindegren, L., et al. 2022, *A&A*, 667, A148

Gallego-Cano, E., Schödel, R., Nogueras-Lara, F., et al. 2020, *A&A*, 634, A71

Generozov, A., & Madigan, A.-M. 2020, *ApJ*, 896, 137

Ghez, A. M., Duchêne, G., Matthews, K., et al. 2003, *ApJL*, 586, L127

Ghez, A. M., Salim, S., Weinberg, N. N., et al. 2008, *ApJ*, 689, 1044

Gillessen, S., Eisenhauer, F., Fritz, T. K., et al. 2009, *ApJL*, 707, L114

GRAVITY Collaboration, Abuter, R., Aimar, N., et al. 2022, *A&A*, 657, L12

Habing, H. J. 1996, *A&A Rv*, 7, 97

Hansen, B. M. S., & Phinney, E. S. 1997, *MNRAS*, 291, 569

Harris, C. R., Millman, K. J., van der Walt, S. J., et al. 2020, *Nature*, 585, 357.

<https://doi.org/10.1038/s41586-020-2649-2>

Hills, J. G. 1988, *Nature*, 331, 687

Hoang, B.-M., Naoz, S., & Sloneker, M. 2022, *ApJ*, 934, 54

Hobbs, G., Lorimer, D. R., Lyne, A. G., & Kramer, M. 2005, *MNRAS*, 360, 974

Hosek, Jr., M. W., Do, T., Martinez, G. D., et al. 2025, *ApJ*, 989, 79

Hosek, Jr., M. W., Lu, J. R., Anderson, J., et al. 2015, *ApJ*, 813, 27

—. 2018, *ApJ*, 855, 13

Hunter, J. D. 2007, *Computing in Science & Engineering*, 9, 90

Jurado, C., Naoz, S., Lam, C. Y., & Hoang, B.-M. 2024, *ApJ*, 971, 95

Kemball, A. J. 2007, in *Astrophysical Masers and their Environments*, ed. J. M. Chapman & W. A. Baan, Vol. 242, 236–245

Kenyon, S. J., Bromley, B. C., Geller, M. J., & Brown, W. R. 2008, *ApJ*, 680, 312

Koposov, S. E., Boubert, D., Li, T. S., et al. 2020, *MNRAS*, 491, 2465

Kormendy, J., & Ho, L. C. 2013, *ARA&A*, 51, 511

Launhardt, R., Zylka, R., & Mezger, P. G. 2002, *A&A*, 384, 112

Li, J., An, T., Shen, Z.-Q., & Miyazaki, A. 2010, *ApJL*, 720, L56

Lu, C. X., & Naoz, S. 2019, *MNRAS*, 484, 1506

Mastrobuono-Battisti, A., Church, R. P., & Davies, M. B. 2021, *MNRAS*, 505, 3314

Menten, K. M., Reid, M. J., Eckart, A., & Genzel, R. 1997, *ApJL*, 475, L111

Moe, M., & Di Stefano, R. 2017, *ApJS*, 230, 15

Neumayer, N., Seth, A., & Böker, T. 2020, *A&A Rv*, 28, 4

Paine, J., & Darling, J. 2022, *ApJ*, 927, 181

Plewa, P. M., Gillessen, S., Eisenhauer, F., et al. 2015, *MNRAS*, 453, 3234

Reid, M. J. 2002, in *IAU Symposium*, Vol. 206, *Cosmic Masers: From Proto-Stars to Black Holes*, ed. V. Migenes & M. J. Reid, 506

Reid, M. J., & Brunthaler, A. 2004, *ApJ*, 616, 872

—. 2020, *ApJ*, 892, 39

Reid, M. J., Menten, K. M., Genzel, R., et al. 2003, *ApJ*, 587, 208

Reid, M. J., Menten, K. M., Trippe, S., Ott, T., & Genzel, R. 2007, *ApJ*, 659, 378

Rose, S. C., Lombardi, Jr., J. C., González Prieto, E., Kiroğlu, F., & Rasio, F. A. 2025, arXiv e-prints, arXiv:2511.01811

Rose, S. C., & MacLeod, M. 2024, ApJL, 963, L17

Rose, S. C., & Mockler, B. 2025, ApJL, 985, L40

Rose, S. C., Naoz, S., Gautam, A. K., et al. 2020, ApJ, 904, 113

Rose, S. C., Naoz, S., Sari, R., & Linial, I. 2023, ApJ, 955, 30

Rossi, E. M., Kobayashi, S., & Sari, R. 2014, ApJ, 795, 125

Sakai, S., Lu, J. R., Ghez, A., et al. 2019, ApJ, 873, 65

Sana, H., de Mink, S. E., de Koter, A., et al. 2012, Science, 337, 444

Sari, R., Kobayashi, S., & Rossi, E. M. 2010, ApJ, 708, 605

Schödel, R., Feldmeier, A., Kunneriath, D., et al. 2014, A&A, 566, A47

Schödel, R., Nogueras-Lara, F., Gallego-Cano, E., et al. 2020, A&A, 641, A102

Schödel, R., Ott, T., Genzel, R., et al. 2002, Nature, 419, 694

Sormani, M. C., Magorrian, J., Nogueras-Lara, F., et al. 2020, MNRAS, 499, 7

Trippe, S., Gillessen, S., Gerhard, O. E., et al. 2008, A&A, 492, 419

Tsuboi, M., Tsutsumi, T., Miyawaki, R., & Miyoshi, M. 2025, PASJ, 77, 733

Verberne, S., Rossi, E. M., Koposov, S. E., et al. 2025, arXiv e-prints, arXiv:2502.17165

Virtanen, P., Gommers, R., Oliphant, T. E., et al. 2020, Nature Methods, 17, 261

Xu, S., Zhang, B., Reid, M. J., et al. 2022, arXiv e-prints, arXiv:2210.03390

Yu, Q., & Tremaine, S. 2003, ApJ, 599, 1129

Zhang, E., Naoz, S., & Will, C. M. 2023, ApJ, 952, 103

Zhu, Q., Kudritzki, R. P., Figer, D. F., Najarro, F., & Merritt, D. 2008, ApJ, 681, 1254

Zubovas, K., Wynn, G. A., & Gualandris, A. 2013, ApJ, 771, 118

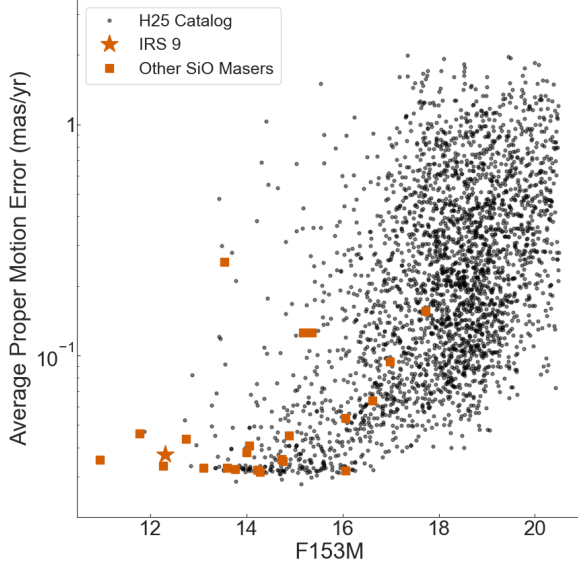


Figure 6. HST proper motion error as a function of magnitude for the SiO masers compared to the HST catalog of astrometric reference stars within $R \leq 25''$ from H25. IRS 9 is highlighted as a red star while the other masers are denoted as red squares. The masers exhibit a median proper motion error of $0.038 \text{ mas yr}^{-1}$ across the sample.

APPENDIX

A. AN HST PROPER MOTION CATALOG OF SIO MASERS NEAR THE GC

The HST proper motions and updated 3D velocities of the 23 SiO masers examined in this study is presented in Table 1. Proper motions are obtained using the same methodology as H25 (see their §3.2), which utilizes Gaussian Processes to simultaneously model systematic errors in the astrometry, if the data requires it. The parameters of the proper motion fits are reported as:

$$\delta_{\alpha^*}^s(t) = \delta_{\alpha_0^*}^s + \mu_{\alpha^*}^s(t - t_0) \quad (\text{A1})$$

$$\delta_{\delta}^s(t) = \delta_{\delta_0}^s + \mu_{\delta}^s(t - t_0), \quad (\text{A2})$$

where $(\delta_{\alpha_0^*}^s, \delta_{\delta_0}^s)$ is the projected position of the star relative to SgrA* at time t_0 and $(\mu_{\alpha^*}^s, \mu_{\delta}^s)$ is the proper motion of the star relative to SgrA*. The proper motion errors for the masers are generally consistent with those obtained for stars at similar magnitudes extracted from this dataset (Figure 6, H25). Additional information provided in Table 1 includes the 3D velocities of the masers (§2.2), the GC escape velocities at their projected radii (§3.1), and their average HST photometry (F127M, F139M, and F153M filters).

Table 1. HST Proper Motion Catalog of SiO Masers

HST ID	Name	r_{2d}	F153M	$\delta_{\alpha_0}^s$	$\sigma_{\delta_{\alpha_0}^s}$	$\delta_{\delta_0}^s$	$\sigma_{\delta_{\delta_0}^s}$	$\mu_{\alpha_*}^s$	$\sigma_{\mu_{\alpha_*}^s}$	μ_{δ}^s	$\sigma_{\mu_{\delta}^s}$	t_0^s	$\sigma_{v_{3d}}$	v_{3d}	$\sigma_{v_{esc,max}}$	$\sigma_{v_{esc,max}}$	Model	Ref
HST_NSC_006749	IRS9	0.33	12.3	5.7087	0.24	-6.3081	0.54	2.95	0.03	2.33	0.03	2018.0060	370.4	1.2	331.1	6.5	2	1
HST_NSC_013716	IRS15NE	0.44	13.5	1.1823	1.71	11.1953	1.32	-1.17	0.29	-6.53	0.22	2019.9712	255.1	8.4	290.4	6.2	5	1
HST_NSC_006721	IRS28	0.47	13.6	10.4958	0.24	-5.8033	0.52	1.29	0.02	-5.52	0.02	2018.2976	224.2	1.1	281.7	6.1	0	1
HST_NSC_013570	IRS7	0.22	11.0	0.0325	0.25	-5.4753	0.53	-0.13	0.03	-4.68	0.03	2016.4545	212.8	3.9	409.9	7.8	0	1
HST_NSC_001500	IRS14NE	0.32	13.1	0.9500	0.24	-8.1693	0.52	3.72	0.02	-3.24	0.02	2018.2453	190.0	1.3	336.5	6.6	0	2
HST_NSC_000182	SiO-18	1.26	14.8	-18.6992	0.26	-26.0982	0.52	-4.22	0.03	0.86	0.02	2018.2458	183.0	1.6	194.5	10.2	2	2
HST_NSC_026835	SiO-24	0.70	15.2	17.1970	0.26	-4.8063	0.54	1.04	0.12	-3.71	0.13	2012.3660	149.2	5.0	237.7	6.8	-1	2
HST_NSC_033541	SiO-28	1.67	16.1	-1.1102	0.28	-42.5594	0.58	0.03	0.04	2.77	0.06	2018.5707	149.0	1.8	182.3	12.2	2	2
HST_NSC_010801	SiO-11	1.58	17.7	1.7632	0.67	40.3025	0.82	2.12	0.15	2.61	0.15	2015.7331	147.2	5.3	184.3	11.8	-1	1
HST_NSC_008236	SiO-6	1.84	11.8	35.2771	0.26	30.7005	0.56	2.57	0.03	2.46	0.05	2018.2828	146.2	1.7	179.3	12.9	2	1
HST_NSC_029882	SiO-14	1.16	14.1	-7.6216	0.28	-28.4695	0.53	2.01	0.04	-0.84	0.03	2018.3923	139.0	1.1	199.3	9.6	2	1
HST_NSC_015582	SiO-25	1.48	17.0	-33.0902	0.70	-17.9272	0.58	-1.58	0.13	-0.92	0.06	2016.5510	137.7	2.3	187.0	11.3	2	2
HST_NSC_001403	IRS12N	0.30	13.8	-3.2758	0.24	-6.9430	0.52	-1.11	0.02	-2.88	0.02	2018.0419	135.1	1.1	347.8	6.8	0	1
HST_NSC_029099	SiO-19	1.06	14.2	16.2528	0.25	-21.6642	0.53	2.70	0.03	1.23	0.02	2017.3928	117.6	1.3	204.4	9.0	0	2
HST_NSC_015623	SiO-15	0.65	14.3	-12.4686	0.23	-11.0668	0.52	-2.50	0.02	0.61	0.02	2018.2361	105.2	1.3	244.5	6.6	0	1
HST_NSC_041830	IRS19NW	0.92	15.4	-14.5725	0.62	-18.4733	0.80	1.16	0.12	-0.56	0.13	2018.3295	97.9	2.4	214.2	8.1	2	1
SiO-27		1.54	16.1	-19.9358	0.23	33.6746	0.52	-0.26	0.02	-1.76	0.02	2017.4084	94.2	1.1	185.4	11.6	0	2
HST_NSC_006677	IRS10EE	0.34	16.6	7.6851	0.32	4.1758	0.56	-0.13	0.06	-2.31	0.06	2018.1952	92.9	2.3	326.7	6.5	0	1
HST_NSC_006624	IRS17	0.56	12.3	13.1282	0.24	5.5455	0.52	-1.08	0.03	-0.93	0.02	2018.4157	92.3	1.0	261.3	6.3	0	1
HST_NSC_057116	SiO-20	0.97	14.9	-13.8596	0.29	20.3505	0.54	0.53	0.04	-1.81	0.04	2018.4570	74.3	1.6	210.9	8.4	-1	2
HST_NSC_000852	SiO-16	1.71	14.7	-26.4149	0.22	-34.4759	0.54	0.17	0.02	-1.72	0.04	2018.4280	66.9	1.5	181.6	12.4	2	1
HST_NSC_002770	SiO-22	1.73	12.7	41.4090	0.26	15.1808	0.55	0.23	0.03	1.22	0.04	2018.2940	58.7	1.5	181.1	12.5	2	2
HST_NSC_018669	SiO-21	1.82	14.0	40.9060	0.26	-22.0445	0.53	0.23	0.03	0.67	0.03	2018.4593	30.5	1.2	179.5	12.8	0	2

NOTE—Description of columns: *HST ID*: HST Catalog Name, *Name*: Maser Name, r_{proj} : Projected radius of star from SgrA*, *F153M*: Average F153M mag., $\delta_{\alpha_*}^s$, $\delta_{\delta_0}^s$: star position at t_0^s relative to SgrA*, $\sigma_{\delta_{\alpha_*}^s}$, $\sigma_{\delta_{\delta_0}^s}$: error in star position at t_0^s , $\mu_{\alpha_*}^s$, μ_{δ}^s : star proper motion relative to SgrA*, $\sigma_{\mu_{\alpha_*}^s}$, $\sigma_{\mu_{\delta}^s}$: error star proper motion, t_0^s : reference epoch of proper motion fit, v_{3d} , $\sigma_{v_{3d}}$: Value and uncertainty of 3D velocity relative to SgrA*, $v_{esc,max}$, $\sigma_{v_{esc,max}}$: Value and uncertainty of v_{esc} at r_{2d} , *Model*: HST kinematic model used – 0: *poly-only*, 1: *poly+step*, 3: *poly+sqexp*, 2: *poly+conf*, 5: *poly+add*, 5: *poly+step* (see H25), *Ref*: Radio proper motion reference – 1: D23, 2: P22

Note—The table is also provided in machine-readable format.

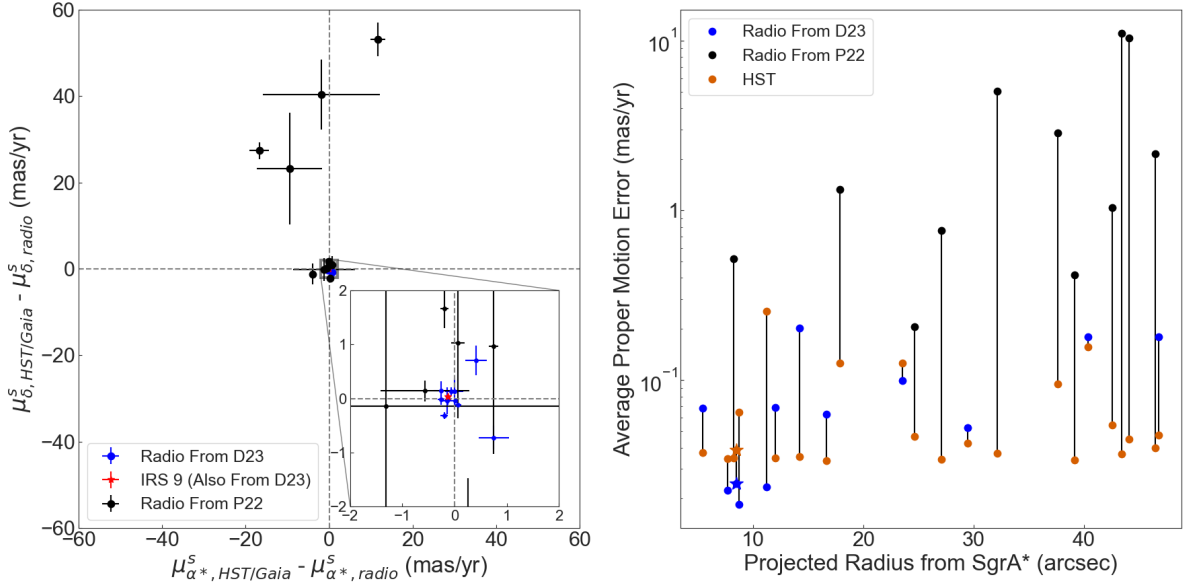


Figure 7. A comparison of the HST and radio proper motion measurements for the masers (left panel) and their corresponding uncertainties (right panel). Left: The measurements show good agreement for the masers with radio measurements from D23 (blue points), but show larger discrepancies for those from P22 (black points). Particularly large discrepancies ($\gtrsim 20$ mas yr $^{-1}$) are found for SiO-16, SiO-21, and SiO-25. Right: The HST proper motion errors (red points) are lower for many sources, especially for those at larger distances where less radio astrometry is available ($R \gtrsim 20''$). Vertical black lines connect the HST and radio proper motion errors for the same source. In both panels, IRS 9 is highlighted with a star symbol.

B. COMPARING THE HST AND RADIO PROPER MOTION MEASUREMENTS OF THE MASERS

The radio proper motion measurements adopted for the 23 masers are taken from D23 and P22. Of the sample, 12 of the sources originate from D23, which defines the most recent radio-based astrometric reference frame for the GC. These sources are primarily close to SgrA* ($r_{2d} \lesssim 20''$) and are among the best-measured sources, with a history of radio astrometric measurements that extends over a ~ 26 year time baseline (Reid et al. 2003, 2007). The radio measurements for the remaining 11 sources comes from P22, whose observations extend over a larger field and thus the sources are mostly at larger radii ($r_{2d} \gtrsim 20''$). These sources generally have fewer radio-based astrometric measurements. The radio reference used for each maser is noted in Table 1.

A comparison between the HST and radio proper motion measurements is shown in the left panel of Figure 7. The agreement between the measurements for the D23 masers is quite good. As discussed in detail by H25, the HST and radio proper motion measurements for the D23 sources are consistent to within 0.041 mas yr $^{-1}$ at 99.7% confidence. IRS 9 is a part of this sample. However, much larger discrepancies are found for many of the P22 masers, most notably for the proposed high-velocity sources SiO-16, SiO-21, and SiO-25, which show discrepancies of $\gtrsim 20$ mas yr $^{-1}$. As noted by P22, this is likely due to the limited radio astrometry available for these sources, which were only measured in 2 radio epochs spanning a ~ 2 year time baseline.

The HST and radio proper motion uncertainties are compared in the right panel of Figure 7. Overall, the HST measurements are more precise for 17 of the masers, and the median HST proper motion error across the sample is ~ 4.5 times smaller than the median radio proper motion error (0.038 mas yr $^{-1}$ vs. 0.18 mas yr $^{-1}$). The largest improvements are achieved for masers at larger radii from SgrA* ($r_{2d} \gtrsim 20''$), where the HST uncertainties can be $\gtrsim 100$ times smaller than the radio uncertainties. For sources closer to SgrA* ($r_{2d} \lesssim 20''$), the HST and radio measurement uncertainties are more comparable, with the median proper motion error across the sample being only ~ 1.6 times smaller for HST compared to radio (0.03 mas yr $^{-1}$ vs. 0.05 mas yr $^{-1}$).

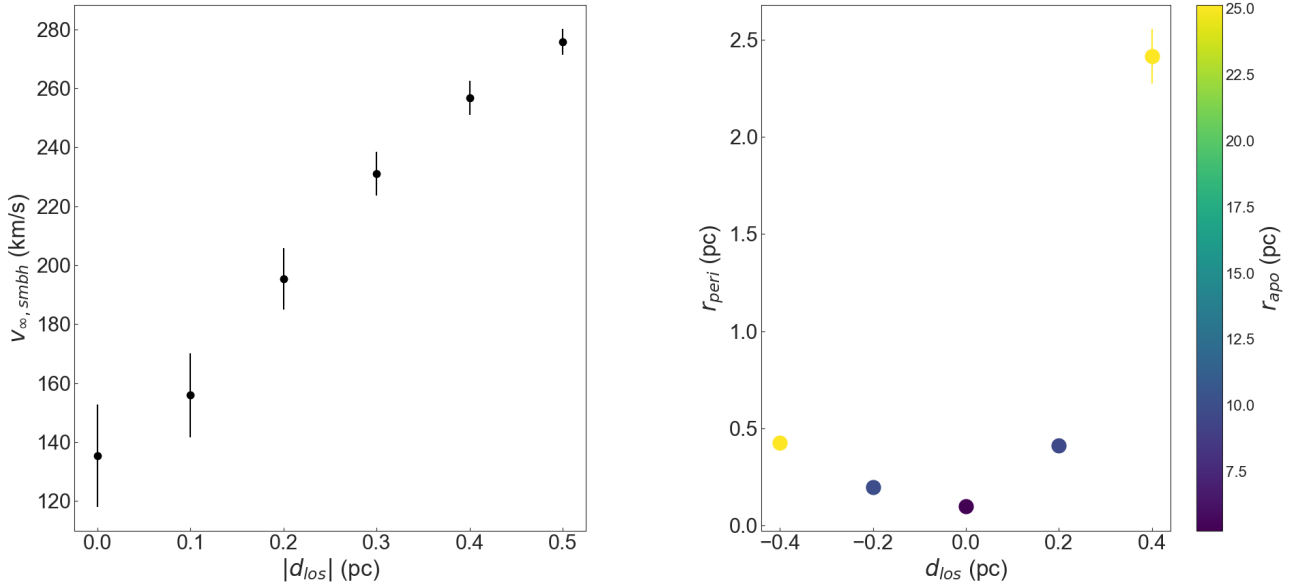


Figure 8. Different calculated properties for the orbit of IRS 9 as a function of d_{los} . *Left:* $v_{\infty,smbh}$ increases as $|d_{los}|$ increases, and so the reported value for the $d_{los} = 0$ pc case ($v_{\infty,smbh} = 134 \pm 18$ km s $^{-1}$) represents a lower limit. *Right:* r_{peri} as a function of d_{los} , with the color of each point corresponding to r_{apo} . The minimum values for r_{peri} and r_{apo} are obtained for the $d_{los} = 0$ pc case, which represents the “tightest” possible orbit for IRS 9 in the GC.

C. ADOPTING DIFFERENT LINE-OF-SIGHT DISTANCES FOR IRS 9

Throughout this paper we assume that d_{los} , the current line-of-sight distance of IRS 9 relative to SgrA*, is 0 pc. In this case, the physical radius of IRS 9 from SgrA* is equal to its projected radius ($r_{2d} = 0.33$ pc), which represents the smallest possible current radius of the star. However, d_{los} is not well constrained for IRS 9. Here we explore how varying d_{los} impacts the results.

In §3.1, we calculate that $v_{\infty,smbh} = 134 \pm 18$ km s $^{-1}$ for IRS 9 in the case where $d_{los} = 0$ pc. If we instead assume a non-zero value for d_{los} , then the current radius of IRS 9 increases, and so the gravitational potential energy (due to SgrA*) becomes less negative. Thus $v_{\infty,smbh}$ increases, for example reaching a value of 276.2 ± 4.4 km s $^{-1}$ for $|d_{los}| = 0.5$ pc (Figure 8, left panel).

We repeat the orbit simulations in §3.2 for d_{los} values of -0.4 pc, -0.2 pc, 0.2 pc, and 0.4 pc. Since the physical radius of IRS 9 is larger in these cases than when $d_{los} = 0$ pc, the periods of the resulting orbits are also larger. For each case, the orbit integrations are calculated for enough time to encompass at least two full orbital periods into the past. For each d_{los} value, the r_{peri} and r_{apo} values derived are larger than the ones obtained when $d_{los} = 0$ pc (Figure 8, middle panel). This shows that the r_{peri} and r_{apo} values derived for the $d_{los} = 0$ pc orbit discussed in the main text of this paper represent lower limits for IRS 9.